LA-UR- 09-00706

Approved for public release;
distribution is unlimited.

Title:	Fully Kinetic Simulations of Magnetic Reconnection in Semi-Collisional Plasmas
Author(s):	William Daughton, X-1-PTA Vadim Roytershteyn, T-15 Brian J. Albright, X-1-PTA Homa Karimabadi, UCSD Lin Yin, X-1-PTA Kevin Bowers, X-1-PTA
Intended for:	submitted to Physics of Plasmas February 11, 2009

Los Alamos
NATIONAL LABORATORY
EST. 1943

Form 836 (7/06)

Fully Kinetic Simulations of Magnetic Reconnection in Semi-Collisional Plasmas

W. Daughton[1], V. Roytershteyn[1], B. J. Albright[1], H. Karimabadi[2], L. Yin[1], and Kevin J. Bowers[1]*
[1] *Los Alamos National Laboratory, Los Alamos, NM 87544*
[2] *University of California, San Diego, La Jolla, 92093*
(Dated: February 3, 2009)

The influence of Coulomb collisions on the dynamics of magnetic reconnection is examined using fully kinetic simulations with a Monte-Carlo treatment of the Fokker-Planck collision operator. This powerful first-principles approach offers a bridge between kinetic and fluid regimes, which may prove useful for understanding the applicability of various fluid models. In order to lay the necessary groundwork, the collision algorithm is first carefully benchmarked for a homogeneous plasma against theoretical predictions for beam-plasma interactions and electrical resistivity. Next, the collisional decay of a current layer is examined as a function of guide field, allowing direct comparisons with transport theory for the parallel and perpendicular resistivity as well as the thermoelectric force. Finally, the transition between collisional and collisionless reconnection is examined in neutral sheet geometry. For modest Lundquist numbers $S \lesssim 1000$, a distinct transition is observed when the thickness of the Sweet-Parker layers falls below the ion inertia length $\delta_{sp} \lesssim d_i$. At higher Lundquist number, deviations from the Sweet-Parker scaling are observed due to the growth of plasmoids (secondary-islands) within the elongated resistive layer. In certain cases, this instability leads to the onset of fast reconnection sooner than expected from $\delta_{sp} \approx d_i$ condition. After the transition to fast reconnection, elongated electron current layers are formed which are unstable to the formation of new plasmoids. The structure and time-dependence of the electron diffusion region in these semi-collisional regimes is profoundly different than reported in two-fluid simulations.

PACS numbers: 52.35.Vd, 52.35.Py, 52.65.-y

I. INTRODUCTION

Magnetic reconnection is thought to play an important role in a wide variety of applications, including planetary magnetospheres, the solar corona and laboratory experiments. While in some of these applications the plasmas is highly collisionless, many laboratory experiments [1] are in a semi-collisional regime. Furthermore, it has been suggested that the transition between collisional and collisionless reconnection may play an important role in regulating coronal heating in stars [2–4].

In sufficiently collisional plasmas, the magnetohydrodynamic (MHD) description should provide a reasonably accurate description of the reconnection dynamics. Within the MHD model, fast steady-state solutions of the Petschek-type are only possible when the resistivity is enhanced within the diffusion region [5–7] by postulating some unknown kinetic process. For spatially uniform resistivity, the MHD model gives rise to the classic Sweet-Parker (SP) solution in which the reconnection rate scales as $S^{-1/2}$ where S is the Lundquist number. In regimes relevant to the solar corona $S \sim 10^8 - 10^{12}$, the implied reconnection rates are far too slow to explain observations. However, the physical relevance of the SP scaling is highly questionable for these parameter regimes, since the elongated layers are unstable to plasmoid (secondary-island) formation [5, 8, 9] at rather modest Lundquist numbers $S \sim 2000$. Recent linear theory predicts that plasmoid formation within SP layers is increasingly violent at higher Lunduist number [10] and simulation suggest this process may lead to a much faster turbulent reconnection scenario [11].

When the thickness of the resistive layer approach the ion kinetic scale, additional physics beyond MHD is crucially important. In neutral sheet geometry, two-fluid theory and simulations indicate an abrupt transition to fast reconnection [12–14] when the thickness of the SP current layer δ_{sp} falls below the ion inertial length d_i. This so-called *Hall or fast regime* has attracted considerable attention since it offers a potential explanation for both the sudden onset of reconnection and the fast rates observed in nature. Within this regime, it has been reported [15–18] that the steady-state reconnection rate is controlled by the ions and is insensitive to the electron physics. However, the precise role of electron physics remains controversial even within two-fluid models [19].

In the collisionless limit, fully kinetic particle-in-cell (PIC) simulations offer a first-principles description of magnetic reconnection. Until recently, PIC simulations [20, 21] were thought to be roughly consistent with the two-fluid simulations. However, more recent large-scale PIC simulations have demonstrated that the structure of the reconnection layer is quite different [22, 23]. In particular, the electron diffusion region forms an elongated current sheet with a complicated two-scale structure [23, 24]. These elongated electron layers are unstable to plasmoid formation leading to a time-dependent reconnection process in which electron physics appears to play an important role [22, 23, 25].

These results have raised fundamental questions regarding the essential physics of reconnection and the ap-

*Guest Scientist. Currently with D. E. Shaw Research,LLC, New York, NY 10036.

plicability of fluid models to describe the correct structure and time-dependent behavior. Typically, fluid theory is better justified in collisional regimes where the gradient scale lengths are large in comparison to the various kinetic scales. While a range of different two-fluid models have been proposed to describe magnetic reconnection, the parameter regimes where these models are valid has never been rigorously established.

In order to address these issues, this work employs a Monte-Carlo approach [26] to directly solve the underlying plasma kinetic equation, which forms the theoretical basis for all reduced fluid descriptions. Although computationally expensive, this well-developed technique describes a full Fokker-Planck collision operator and thus permits a first-principles study of the transition from collisional Sweet-Parker regimes into the faster kinetic regime. This approach allows direct comparison with reduced fluid models regarding the onset criteria as well as the structure and stability of the diffusion region.

To our knowledge, this manuscript represents the first attempt to apply this technique to the problem of magnetic reconnection. Thus before proceeding, we first review some essential background information necessary for understanding this method. Next, to ensure that the collision algorithm is properly implemented, a series of benchmarks are performed against theoretical predictions from classical transport theory. These problems include the slowing down and diffusion of test particles, the electrical resistivity of a homogeneous unmagnetized plasma and the collisional decay of a current layer. This last problem permits detailed comparison with theoretical predictions [27] for the collisional momentum exchange between ions and electrons. These benchmarks establish that Coulomb collisions are introduced in a well-controlled manner; thus allowing the initial resistivity to be chosen as desired. Furthermore, the physical treatment of Coulomb collisions includes a range of complexities not typically considered within fluid simulations. These effects include parallel and perpendicular resistivities that vary in space and time due to electron Ohmic heating and a significant contribution from the thermal force on the edge of the current layer.

After establishing the necessary groundwork, this paper examines the transition between collisional and collisionless reconnection in neutral sheet geometry. In sufficiently collisional regimes, this fully kinetic approach recovers the Sweet-Parker solution from resistive MHD. Furthermore, in modest sized systems $\sim 100 d_i$ a transition to faster reconnection is observed when $\delta_{sp} \leq d_i$, in agreement with two-fluid predictions [12–14]. However, in somewhat larger systems $\sim 200 d_i$, the resistive layers are unstable to the formation of magnetic islands and this leads to a transition somewhat sooner than expected from the $\delta_{sp} \leq d_i$ condition. After the transition, elongated electron current layers are always observed in these semi-collisional kinetic simulations. In comparison to the collisionless limit [20, 23], the thickness of the electron layer is somewhat broader $\sim 30\%$ near the x-point while the electron outflow jets open sooner and are $\sim 50\%$ wider near the location of maximum outflow. For most of the simulations performed, the elongated electron layers are unstable to plasmoid formation leading to a time-dependent reconnection process similar to recent collisionless results [22, 23, 25]. Both the structure and time-dependence of these results are dramatically different than reported in two-fluid simulations, indicating a need to reconsider the physics required to correctly describe the electron layer.

II. BACKGROUND AND METHODS

For weakly correlated non-relativistic parameter regimes, the theoretical framework for most of plasma physics is based on the following kinetic equation

$$\frac{\partial f_s}{\partial t} + \mathrm{v} \cdot \frac{\partial f_s}{\partial \mathbf{x}} + \frac{q_s}{m_s}\left(\mathbf{E} + \frac{\mathbf{v}\times\mathbf{B}}{c}\right)\cdot\frac{\partial f_s}{\partial \mathbf{v}} = \sum_{s'} C_{ss'} \ , \quad (1)$$

where $f_s(\mathbf{x},\mathbf{v},t)$ is the single particle distribution function for species s and $C_{ss'}$ is an operator describing binary Coulomb collisions between species s and s'. For weakly coupled plasmas, this term is well approximated by the Fokker-Planck collision operator[28]

$$\frac{C_{ss'}}{\Gamma_s} = -\frac{\partial}{\partial v_\alpha}\left(f_s \frac{\partial h_{s'}}{\partial v_\alpha}\right) + \frac{1}{2}\frac{\partial^2}{\partial v_\alpha \partial v_\beta}\left(f_s \frac{\partial^2 g_{s'}}{\partial v_\alpha \partial v_\beta}\right) \ , \quad (2)$$

where $\Gamma_s = 4\pi e^4 \ln\Lambda / m_s^2$, each species has charge e and mass m_s, there is an implied summation over Cartesian indices (α, β), and

$$h_{s'}(\mathbf{v}) = \left(1 + \frac{m_s}{m_{s'}}\right)\int \frac{f_{s'}(\mathbf{v}')}{|\mathbf{v}-\mathbf{v}'|} d\mathbf{v}' \ , \quad (3)$$

$$g_{s'}(\mathbf{v}) = \int f_{s'}(\mathbf{v}')|\mathbf{v}-\mathbf{v}'| d\mathbf{v}' \ . \quad (4)$$

It can be shown that Eq. (2) is equivalent to the collision operator first derived by Landau [29]. In a classical plasma, the so-called Coulomb logarithm is given by $\ln\Lambda \approx \ln\left(12\pi n_e \lambda_D^3\right)$, where λ_D is the Debye length. Assuming the distribution functions are close to Maxwellian, the characteristic collision frequency between species s and s' is given by [30]

$$\nu_{ss'} = \frac{16\sqrt{\pi}}{3}\frac{n_{s'} e^4 \ln\Lambda}{m_s m_{ss'}\left(v_{ths}^2 + v_{ths'}^2\right)^{3/2}} \ , \quad (5)$$

where $v_{ths} = (2T_s/m_s)^{1/2}$ is the thermal velocity of species s with temperature T_s and $m_{ss'} = m_s m_{s'}/(m_s + m_{s'})$ is the reduced mass for the binary collision. This generalized expression is equivalent to the collision frequencies defined in the classic Braginskii review [27].

Previous studies of magnetic reconnection have focused on either the collisionless limit where the operator $C_{ss'}$ in Eq. (1) is neglected entirely, or have employed a variety

of simplified moment descriptions. For sufficiently collisional regimes, a multi-fluid description of the plasma can be rigorously derived [27] from Eq. (1) and with additional approximations these fluid equations can be further simplified to the resistive magnetohydrodynamic (MHD) model. In the present study, the full kinetic equation (1) is solved using the particle-in-cell code VPIC [31] which was recently modified to include Coulomb collisions using the Takizuka-Abe particle-pairing algorithm [26]. For the regimes of interest, the electron collision frequency is small in comparison to the electron plasma frequency $\nu_{ei} \ll \omega_{pe}$, and thus the kinetic equation may be solved by an operator splitting technique in which the particles are advanced in time using the self-consistent fields in the same manner as in the collisionless limit [31]. In order to include the influence of weak collisions, periodically the particles within each cell ($\sim$1 Debye length) are randomly paired and scattered in velocity space to mimic the Coulomb cross-section[26]. The scattering angle Θ for a collision between species s and s' is chosen in the center of mass frame using the random variable $\zeta \equiv \tan(\Theta/2)$, where ζ is randomly selected from a Gaussian distribution with zero mean $\langle\zeta\rangle = 0$ and variance

$$\langle\zeta^2\rangle = \frac{2\pi e^4 n_s \ln\Lambda}{m_{ss'}^2 |\mathbf{v}_s - \mathbf{v}_{s'}|^3}\Delta t_{col} \ , \tag{6}$$

where Δt_{col} is the time step for the collision operation. This procedure is repeated for both inter-species and cross-species collisions. Since the collisions are treated pairwise, exact conservation of energy and momentum is guaranteed. While the basic time step for the explicit PIC particle advance Δt_{pic} must resolve the Courant condition and the plasma frequency ω_{pe}, it is usually possible to sub-cycle the collision operation provided that $\nu_{ei}\Delta t_{col} \ll 1$. In this limit, it can be rigorously demonstrated that the Monte-Carlo procedure is equivalent to the full Fokker-Planck operator [26, 32]. In practice, good convergence is obtained with $\nu_{ei}\Delta t_{col} \lesssim 0.03$ which still permits fairly aggressive sub-cycling of the collision algorithm in weakly collisional $\nu_{ei} \ll \omega_{pe}$ regimes. In highly collisional regimes, the particle-pairing algorithm is quite expensive and more efficient methods are available (see Ref. [33] and references therein).

III. COLLISIONAL BENCHMARKS

In the collisionless limit, the VPIC code has been benchmarked for reconnection studies by detailed comparisons with the linear Vlasov theory and extensive cross-verification studies with other PIC codes. The particle-pairing collision algorithm within VPIC was recently benchmarked for the problem of temperature relaxation between species [33]. In this section, new collisional benchmarks are presented for a number of problems directly relevant to reconnection physics.

A. Slowing Down and Diffusion of a Test Beam

Many of the basic features of the collisional plasma transport coefficients are determined by the strong v^{-4} dependence on the relative velocity in the Coulomb cross section. In order to verify this physics, one of the simplest and most basic test problems is the slowing down and diffusion of an electron test beam propagating through a uniform background plasma. The initial distribution of the electron beam is cold

$$f_0^B = n_b \delta(\mathbf{v} - v_o \mathbf{e}_x) \ , \tag{7}$$

where n_b is the beam density and v_o is the initial beam velocity. Three characteristic relaxation rates are typically [30] defined

$$\nu_s = \frac{1}{v_o}\frac{\mathrm{d}}{\mathrm{d}t}\langle v - v_o\rangle \ , \tag{8}$$

$$\nu_\parallel = \frac{1}{v_o^2}\frac{\mathrm{d}}{\mathrm{d}t}\langle (v_\parallel - v_o)^2\rangle \ , \tag{9}$$

$$\nu_\perp = \frac{1}{v_o^2}\frac{\mathrm{d}}{\mathrm{d}t}\langle v_\perp^2\rangle \ , \tag{10}$$

where ν_s is the slowing down rate of the beam, $\nu_\parallel$ and $\nu_\perp$ are the velocity space diffusion rates parallel and perpendicular to the direction of the beam propagation and $\langle\ \rangle$ refers to an average over the test particle distribution. Simple analytic expressions for these relaxation rates may be computed from Fokker-Planck theory [30] by neglecting the interactions between the test particles. For a uniform Maxwellian background plasma with density n_o and temperature $T_i = T_e$, the resulting expressions are

$$\nu_s = \frac{2\Gamma_e}{v_o}\sum_s \frac{n_s}{v_{ths}^2}\left(1 + \frac{m_e}{m_s}\right) G(v_o/v_{ths}) \ , \tag{11}$$

$$\nu_\parallel = \frac{2\Gamma_e}{v_o^3}\sum_s n_s G(v_o/v_{ths}) \ , \tag{12}$$

$$\nu_\perp = \frac{2\Gamma_e}{v_o^3}\sum_s n_s \left[\Phi(v_o/v_{ths}) - G(v_o/v_{ths})\right] \ , \tag{13}$$

where the sum $s = i, e$ is over the background and

$$\Phi(x) = \frac{2}{\pi^{1/2}}\int_0^x \mathrm{d}\xi e^{-\xi^2} \ ,$$

$$G(x) = \frac{\Phi(x) - x\Phi'(x)}{2x^2} \ .$$

In order to test the collision algorithm against the theoretical predictions (11)-(12), a series of simulations were performed with a uniform hydrogen plasma with density $n_o = 10^{18}$ cm^{-3}, temperature $T_e = T_i = 20$ eV and $\ln\Lambda = 10$. In addition, a population of test electrons with the initial beam distribution (7) was included. The beam velocity was varied over the range $v_o/v_{the} = 0.2 \rightarrow 3$ with a beam density of $n_B = 0.01 n_o$. The simulation domain was $(2 \times 3 \times 3)$ cells, with the cell size equal to the Debye

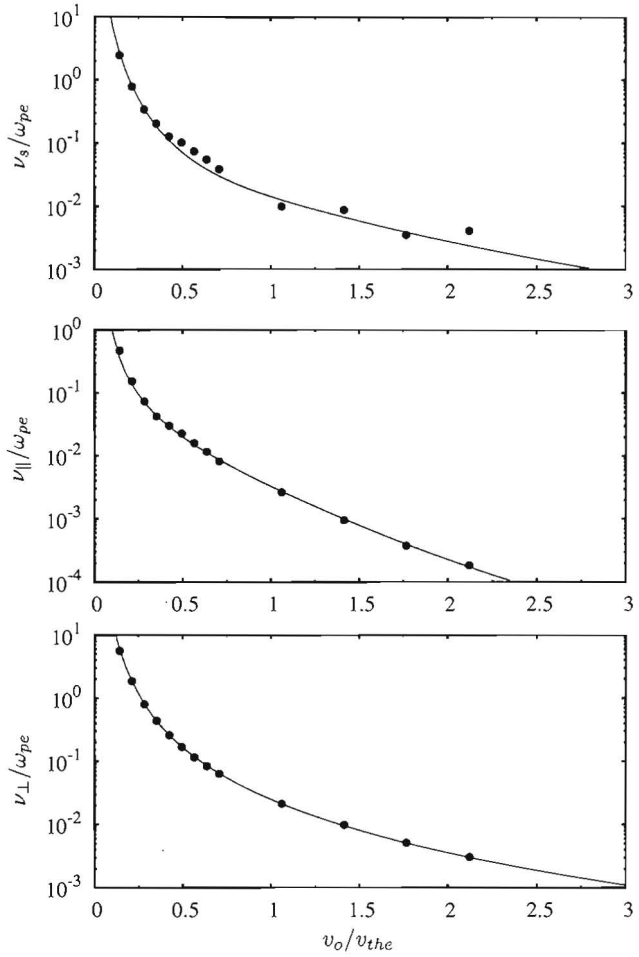

FIG. 1: Comparison of theory against simulation for the slowing down rate (top), parallel diffusion rate (middle), and perpendicular diffusion rate (bottom) as a function of the initial electron beam speed v_o. The continuous lines are the theoretical predictions in Eqns. (11)-(12) and the points represent the rate measured in the kinetic simulations.

length. The simulations used 10,000 particles per cell and the collision operator was applied every PIC time step. To more accurately compare the simulation results with the theoretical predictions, the collisions between the test particles in the electron beam were ignored. The collisions between test particles and the background, as well as the collisions within and between the background species were included. The quantities $\langle v - v_o \rangle$, $\langle (v_{\|} - v_o)^2 \rangle$ and $\langle v_{\perp}^2 \rangle$ were computed for the test particles at each simulation time step and the initial time evolution was fit to a linear function to extract the relaxation rates in Eqns. (8)-(10). As shown in Fig. 1, the simulation results are in excellent agreement with the theoretical predictions for the relaxation rates in Eqns. (11)-(12). These results demonstrate that the collision algorithm is accurately capturing the strong velocity space dependence over a broad range of parameters.

B. Electrical Resistivity in Homogeneous Plasma

In order to interpret kinetic simulations of magnetic reconnection, it is important to verify that the collisional resistivity follows the expected theoretical form. In this section, the simplest case of a homogenous unmagnetized plasma is considered. For a given set of plasma parameters, the resistivity is calculated by imposing an electric field between two parallel plates and measuring the resulting saturation current. These benchmarks are performed in small system ($1 \times 3 \times 3$ cells) with a cell size equal to the Debye length and 50,000 particles per cell. The boundary conditions are periodic in y and z for both particles and fields, while in the x-direction the electric field E_x is applied and the particle boundary condition is periodic. In order to obtain a clean saturation, the applied electric field must be small in comparison to the runaway [34] field $E_{cr} \approx (m_e T_e)^{1/2} \nu_{ee}/e$ where ν_{ee} is the electron-electron collision frequency from Eq. (5). In this parameter regime, the collision algorithm recovers the well-known Spitzer resistivity to an accuracy of approximately $\sim 3\%$. A typical example of the measured current as a function of time is illustrated in Fig. 2 for a hydrogen plasma at $T = 20$ eV, density $n = 10^{18}$ cm^{-3} and applied electric field $E/E_{cr} = 0.1$. The expected saturation current is given by $J_o = E/\eta_{sp}$ where $\eta_{sp} = 0.51 m_e \nu_{ei}/(e^2 n_e)$ is the Spitzer resistivity for hydrogen and ν_{ei} is evaluated with the actual electron temperature to account for the weak Ohmic heating in the simulation. While the primary physics of electrical resistivity involves the momentum exchange due to electron-ion collisions, the numerical coefficient 0.51 is determined by the relative importance of electron-electron collisions which control the shape of the distorted electron distribution within the applied electric field. The precise quantitative agreement in Fig. 2 demonstrates that the collisional operator within VPIC is properly capturing this delicate interplay. It should be noted that for applied electric fields comparable to the runaway limit $E \gtrsim E_{cr}$, no steady-state solution is found. This feature of the collisional momentum exchange is important to properly describe semi-collisional regimes where the reconnection electric field can easily exceed the runaway limit.

This example benchmark illustrates the level of accuracy that can be achieved with the particle pairing collision algorithm. However, in order to apply the collision operator to large-scale reconnection problems, there are several additional subtleties that must be considered. First, while it is possible to use the realistic hydrogen mass ratio $m_i/m_e = 1836$ in small benchmarks, large-scale reconnection simulations are only possible with a reduced mass ratio. In addition, the functional form of the resistive term is more complicated in a magnetized plasma and within current sheet geometry it is possible for other terms such as the thermoelectric force to play a role in the momentum balance. In the next section, these effects are systematically examined.

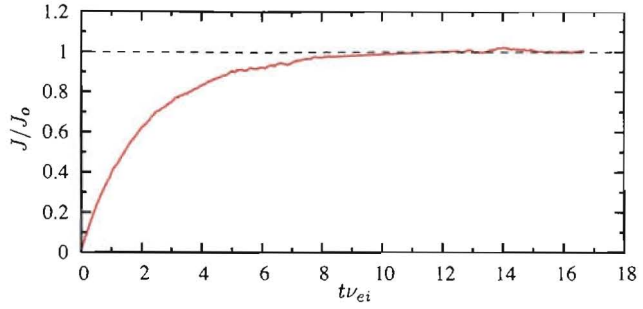

FIG. 2: Example resistivity benchmark showing current as a function of time between two parallel plates with an applied electric field. The parameters are for hydrogen at $T = 20$ eV, $n = 10^{18}$ cm^{-3} and $E/E_{cr} = 0.1$. The saturation current $J_o = E/\eta_{sp}$ is in excellent agreement with Spitzer theory.

C. Collisional Decay of a Current Layer

1. *Theoretical Background*

For reconnection physics, the so-called generalized Ohm's law plays a crucial role in determining how the frozen-flux condition is violated within the diffusion region. This relationship may be be rigorously derived from the first moment of Eq. (1) for the electrons

$$n_e m_e \frac{d\mathbf{U}_e}{dt} + \nabla \cdot \mathbf{P}_e + en_e \left(\mathbf{E} + \frac{\mathbf{U}_e \times \mathbf{B}}{c} \right) = \mathbf{R}_e \ , \quad (14)$$

where n_e is the density, $\mathbf{U}_e$ is the electron fluid velocity, $\mathbf{P}_e$ is the pressure tensor and $\mathbf{R}_e$ is the first velocity moment of the collision operator, corresponding to the collisional momentum exchange between electrons and ions. For sufficiently collisional plasmas with weak spatial gradients, both $\mathbf{R}_e$ and off-diagonal terms of $\mathbf{P}_e$ can be calculated from transport theory [27]. The resulting momentum exchange $\mathbf{R}_e = \mathbf{R}_u + \mathbf{R}_T$ is composed of two contributions: the friction force $\mathbf{R}_u$ due to the relative drift between ions and electron and the thermal force $\mathbf{R}_T$. In the limit where the electron cyclotron frequency is large $\Omega_e \equiv eB/(m_e c) \gg \nu_{ei}$, the friction force is

$$\mathbf{R}_u = en_e \left(\eta_\parallel \mathbf{J}_\parallel + \eta_\perp \mathbf{J}_\perp \right) \ , \quad (15)$$

where $\mathbf{J} = en_e(\mathbf{U}_i - \mathbf{U}_e)$ is the current density, η is the resistivity, the subscripts $\parallel$ and $\perp$ are relative to the magnetic field direction (i.e. $\mathbf{J}_\parallel = (\mathbf{b} \cdot \mathbf{J})\mathbf{b}$ and $\mathbf{J}_\perp = \mathbf{b} \times (\mathbf{J} \times \mathbf{b})$ where $\mathbf{b} = \mathbf{B}/B$ is the unit vector in the direction of the magnetic field). The perpendicular resistivity is given by $\eta_\perp = m_e \nu_{ei}/(e^2 n_e)$ while the parallel resistivity for hydrogen $\eta_\parallel \approx 0.51 \eta_\perp$ has the same coefficient as the unmagnetized limit discussed in the previous section. The thermal force in the strongly magnetized limit $\nu_{ei} \ll \Omega_e$ is given by [27]

$$\mathbf{R}_T = -0.71 n_e \nabla_\parallel T_e - \frac{3 n_e \nu_{ei}}{2\Omega_e} \mathbf{b} \times \nabla T_e \ , \quad (16)$$

where the coefficient 0.71 is for hydrogen. Although the thermal electric force $\mathbf{R}_T$ is typically neglected in fluid modeling of reconnection, the second term in Eq. (16) can be non-negligible in layers with significant temperature gradients, as demonstrated later in this section.

As mentioned previously, large-scale reconnection simulations are only feasible at reduced mass ratio. Thus for consistency, in this section we employ the same artificial mass ratio $m_i/m_e = 40$ used in Sec. IV. As mentioned previously, the precise numerical coefficients in Eqns. (15)-(16) are determined by the relative importance of electron-electron and electron-ion collisions. From Eq. (5), the relevant ratio is $\nu_{ei}/\nu_{ee} = \sqrt{2}/(1 + m_e/m_i)^{1/2}$ provided that $T_i = T_e$ and the charge is the same for ions and electrons (i.e $Z = 1$). In comparison to a hydrogen plasma, this ratio is only 1.2% smaller for the artificial electron mass $m_i/m_e = 40$ used in this study, and thus the numerical coefficients should be essentially identical to the hydrogen values [27].

2. *Initial Conditions and Normalizations*

In order to systematically compare these predictions from transport theory against the kinetic simulations, the collisional decay of a current layer is examined for a Harris sheet [35] with initial magnetic field

$$\mathbf{B}(z) = B_o \tanh\left(\frac{z}{\lambda}\right) \hat{\mathbf{x}} + B_y \hat{\mathbf{y}} \ , \quad (17)$$

where B_o is the asymptotic field in the x-direction, B_y is a uniform guide field in the y-direction and λ is the half-thickness of the current sheet. The initial density $n = n_o \mathrm{sech}^2(z/\lambda)$ is provided by drifting Maxwellian distributions with spatially uniform drift velocity $U_{ys} = 2cT_o/(q_s B_o \lambda)$ and uniform initial temperature T_o for both species. The resulting current density is purely in the y-direction $J_y = J_o \mathrm{sech}^2(z/\lambda)$ where $J_o = cB_o/(4\pi\lambda)$. Thus the relative contribution between parallel and perpendicular current can be adjusted by changing the guide field B_y. In order to examine the collisional decay of the layer while avoiding magnetic reconnection or plasma instabilities, we consider a narrow 2D simulation domain $L_x \times L_z = 0.5 d_i \times 8 d_i$ where $d_i = c/\omega_{pi}$ is the ion inertial length and $\omega_{pi} = \sqrt{(4\pi n_o e^2)/m_i}$. The initial sheet half-thickness is $\lambda = 2d_i$ and $\omega_{pe}/\Omega_{eo} = 7$ where $\omega_{pe} = \sqrt{(4\pi n_o e^2)/m_e}$ and $\Omega_{eo} = eB_o/(m_e c)$. These parameters correspond to an electron thermal speed of $v_{the}/c = 0.1$ and the mass ratio is $m_i/m_e = 40$. The spatial grid is 32×512 with 4000 particles per cell for each species and PIC time step is $\omega_{pe}\Delta t_{pic} = 0.069$. The boundary conditions are periodic for both particles and fields in the x-direction, while on the z-boundaries particles are reflected and the field boundary condition is conducting.

For the purpose of this study, it is useful to hold the initial current sheet parameters fixed while independently prescribing the initial resistivity. This is accomplished

by introducing an overall prefactor in Eq. (6) in order to set ν_{ei} as desired, while the relative magnitude of the other collision frequencies follows from Eq. (5). Recall that the resistivity in a plasma is only a function of the electron temperature, which is spatially uniform for the initial Harris sheet. As the simulation proceeds, Ohmic heating (ηJ^2) within the current layer increases the electron temperature, which causes the actual resistivity to vary in both space and time. To facilitate comparison with two-fluid simulations [13], we employ the same normalization for the dimensionless resistivity

$$\hat{\eta}_\perp \equiv \frac{\omega_{pi}^2}{4\pi\Omega_{io}}\eta_\perp = \frac{\nu_{ei}^o}{\Omega_{eo}} = \hat{\eta}_{\perp o}\left(\frac{T_o}{T_e}\right)^{3/2} , \qquad (18)$$

$$\hat{\eta}_\parallel \equiv \frac{\omega_{pi}^2}{4\pi\Omega_{io}}\eta_\parallel = 0.51\frac{\nu_{ei}^o}{\Omega_{eo}} = \hat{\eta}_{\parallel o}\left(\frac{T_o}{T_e}\right)^{3/2} ,$$

where ν_{ei}^o is the electron-ion collision frequency based on n_o the central reference density, $\hat{\eta}_{\perp o}$ and $\hat{\eta}_{\parallel o} = 0.51\hat{\eta}_{\perp o}$ are the initial uniform resistivities at temperature T_o and the local electron temperature is $T_e \approx \mathrm{Tr}(\mathbf{P}_e)/(3n_e)$. As discussed in the following section, this local electron temperature is well-defined for the collisional SP regime.

3. *Collisional Time Scales and Heating*

The initial electron heating rate may be estimated by assuming that the Ohmic heating goes entirely into electron kinetic energy and neglecting all other terms

$$\frac{3}{2}n_e\frac{\partial T_e}{\partial t} \approx \eta_\parallel J_\parallel^2 + \eta_\perp J_\perp^2 . \qquad (19)$$

Assuming the parallel term dominates in the central region and using $J_o = cB_o/(4\pi\lambda)$ for a Harris sheet, the electron heating over an initial time interval τ is roughly

$$\frac{\Delta T_e}{T_o} \approx \frac{8}{3}\left(\frac{d_i}{\lambda}\right)^2 \hat{\eta}_{\parallel o}\,(\tau\Omega_{io}) , \qquad (20)$$

where $\Delta T_e = T_e - T_o$. This expression for the Ohmic electron heating is valid over a short initial interval where the terms neglected in Eq. (19) are small. Over longer times, the layer expands and the ions come into thermal equilibrium with electrons on a time scale $\tau_{eq} \sim (m_i/m_e)\nu_{ei}^{-1}$. For SP reconnection, the transit time for plasma through the diffusion region $\tau_A = L_{sp}/V_A$ is long in comparison to the thermal equilibration time

$$\frac{\tau_A}{\tau_{eq}} \sim \left(\frac{\delta_{sp}}{d_i}\right)^2 . \qquad (21)$$

Electrons and ions both relax to a local Maxwellian on the self-collision time scales (ν_{ee}^{-1} and ν_{ii}^{-1}) which are a factor of m_i/m_e and $(m_i/m_e)^{1/2}$ faster than τ_{eq}. Thus in the SP regime $\delta_{sp} > d_i$, Eq. (21) implies that $T_i \approx T_e$ with both species close to local Maxwellian distributions. Over time scales longer than τ_{eq}, pressure balance

$$\frac{d}{dz}\left[\frac{B^2}{8\pi} + n(T_i + T_e)\right] \approx 0 ,$$

across the resistive SP layer [3] constrains the central temperature to

$$\frac{T_e}{T_o} \approx \frac{T_i}{T_o} \approx \frac{n_o}{n_c}\left[\left(\frac{B_{in}}{B_o}\right)^2 + \frac{n_{in}}{n_o}\right] , \qquad (22)$$

where n_c is the central density and B_{in} and n_{in} are the upstream values of magnetic field and density.

4. *Comparison of Transport Theory with PIC Simulation*

In order to check the predictions from transport theory, the various terms in the electron momentum equation (14) are directly computed in the simulations and time-averaged over a relatively short interval during the initial decay of the layer. Since the predictions from transport theory are valid [27] on a time scale $\tau \gg \nu_{ee}^{-1}$, it is necessary to wait a number of collision times to allow the electron distribution to develop. The terms on the left-hand-side of Eq. (14) are evaluated directly from the PIC simulations while the collisional momentum exchange $\mathbf{R}_e$ is estimated using the theoretical predictions in Eqns. (15)-(16). Although there are no temperature gradients in the initial Harris sheet, electron Ohmic heating gives rise to a $\nabla T_e \times \mathbf{B}$ contribution to the thermal force [see Eq. (16)]. In a Harris sheet, the magnitude of this term relative to the friction force is approximately

$$\left|\frac{\mathbf{R}_T}{\mathbf{R}_u}\right| \sim \frac{3}{4}\left(\frac{B_o}{B_*}\right)\left(\frac{\Delta T_e}{T_o}\right) , \qquad (23)$$

where B_* is the local magnetic field at the location of maximum temperature gradient and the initial heating $\Delta T_e/T_o$ is estimated from Eq. (20).

For the benchmark comparisons, we first consider two simulations with strong guide field $B_y = B_o$ so the strongly magnetized ordering $\nu_{ei} \ll \Omega_e$ is well satisfied across the entire layer. The collision operator was sub-cycled such that $\nu_{ei}^o \Delta t_{col} \approx 0.005$, but the results were essentially indistinguishable for more aggressive sub-cycling up to $\nu_{ei}^o \Delta t_{col} \approx 0.02$. In the first simulation, the initial resistivity is $\hat{\eta}_{\perp o} = 0.03$ and the time average is between $t\nu_{ei}^o = 5 \rightarrow 6.6$ (corresponding to $t\Omega_{io} = 4.2 \rightarrow 5.5$). At the end of this interval, the predicted electron heating from Eq. (20) is $\Delta T_e/T_o \approx 0.056$, is in good agreement with the observed value of 0.06 in the simulation. The temperature gradient is strongest near $z/\lambda \approx 0.3$ corresponding to $B_o/B_* \approx 1$, which from Eq. (23) implies the maximum thermal force is only $\sim 4\%$ of the friction force. In the second simulation, the initial resistivity is $\hat{\eta}_{\perp o} = 0.1$ and time averaged is performed between $t\nu_{ei}^o = 4.3 \rightarrow 7.7$ (corresponding to

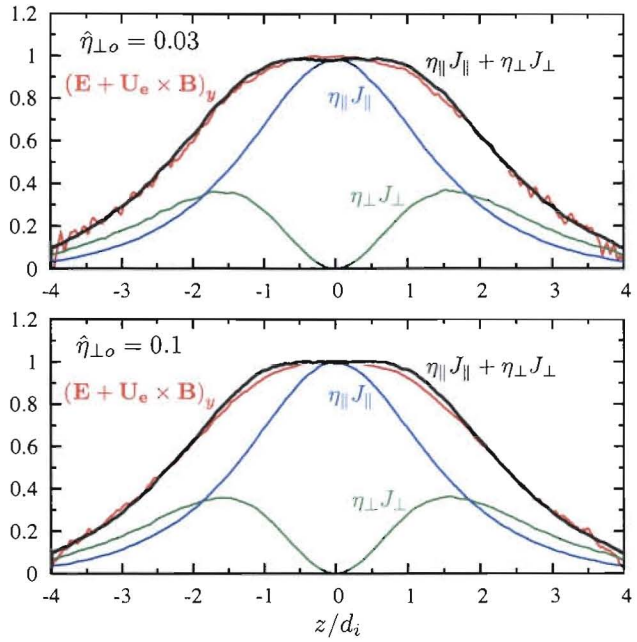

FIG. 3: Force balance in the y-direction across two collisional current sheets with strong guide field $B_y = B_o$, mass ratio $m_i/m_e = 40$, current sheet thickness is $\lambda/d_i = 2$ and perpendicular resistivities $\hat{\eta}_{\perp o} = 0.03$ (top) and $\hat{\eta}_{\perp o} = 0.1$ (bottom). The non-ideal electric field (red) is computed directly from the PIC simulations while the parallel (blue) and perpendicular (green) resistive terms are computed from Eq. (15) using the current density and electron temperature within the simulation. Each term is normalized by $n_o E_y$ at $z = 0$. The total resistive contribution (black) is in good agreement with the non-ideal electric field.

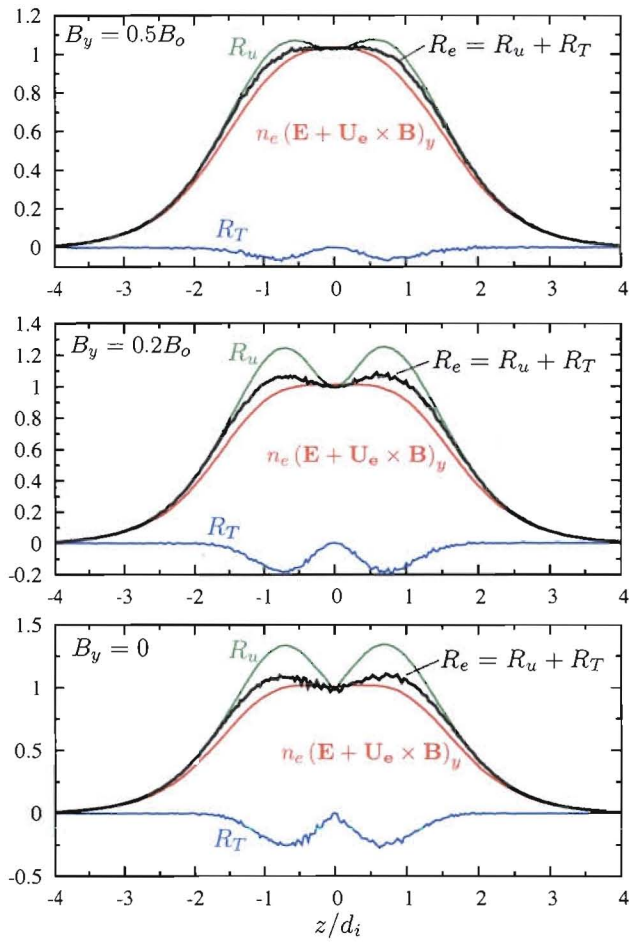

FIG. 4: Force balance in the y-direction across three collisional current sheets with guide field $B_y/B_o = 0.5$ (top), $B_y/B_o = 0.2$ (middle) and $B_y/B_o = 0$ (bottom). The non-ideal electric field (red) is computed directly from the simulations while the friction force R_u (green) and thermal force R_T (blue) are computed from Eq. (A1) and (A2) using the actual simulation conditions ($\mathbf{J}$, $\mathbf{B}$, T_e, n_e). The sum of these two terms (black) corresponds to the total collisional momentum exchange estimated from transport theory. Each term is normalized by $n_o E_y$ at $z = 0$ and parameters are $\hat{\eta}_{\perp o} = 0.1$, $m_i/m_e = 40$, and $\lambda/d_i = 2$.

$t\Omega_{io} = 1.1 \rightarrow 1.93$). The expected heating from Eq. (20) is $\Delta T_e/T_o \approx 0.066$, is in good agreement with the observed value of 0.063. Using $B_o/B_* \approx 1$, this implies the thermal force is again small $\sim 4\%$ in comparison to the friction force. Direct evaluation of the thermal force using Eq. (16) also confirms these estimates, but the statistical fluctuations are comparable to the small off-set. Examining the other terms in the y-component of the momentum balance, both electron inertia and $\nabla\cdot\mathbf{P}_e$ are completely negligible for these ion-scale $\lambda = 2d_i$ layers. The dominant terms in the y-component of Eq. (14) are the inductive electric field E_y and the friction force, with a smaller contribution from $U_{ez}B_x$ due to the weak outward expansion. In Fig. 3, these terms are averaged over the x-direction and shown across each layer. The friction force is evaluated from Eq. (15) using the resistivity in Eq. (18) and the actual moments ($\mathbf{J}$, T_e) for each simulation. At the center of the current sheet, the electric field is balanced entirely by the parallel resistivity $\eta_\parallel J_\parallel$ since the current J_y is purely parallel. On the edge of the layer, the parallel and perpendicular resistive terms are comparable. The agreement between these kinetic simulations and transport theory is quite good, with maximum deviation of $\sim 4\%$ in the region $z \sim d_i$ where the weak thermal force may play some role (not included) and where there are significant gradients in the magnetic that are not included in the theory.

Next we consider the limit of weak guide field, where the strongly magnetized ordering is violated within the central region of layer. The generalization of Eqns. (15)-(16) to arbitrary $\xi \equiv \Omega_e/\nu_{ei}$ is significantly more complicated [27] and is given in Appendix A. These generalized expressions are particularly important for neutral sheet geometry where $\xi \rightarrow 0$ in the center of the layer, while $\xi \gg 1$ in the outer region. The strongly magnetized limit is accurately recovered when $\xi \gtrsim 10$. Thus in a neutral sheet, Eqns. (15)-(16) are appropriate in the outer region

defined by

$$|z| \gtrsim 0.5\lambda \sinh^{-1}(20\hat{\eta}_{\perp o}) \qquad (24)$$

while the generalized expressions in Appendix A must be used in the inner region. In order to further examine the y-component of the momentum balance, we consider three additional simulations with guide field $B_y/B_o = 0.5$, 0.2 and 0. In each case, the initial perpendicular resistivity is $\hat{\eta}_{\perp o} = 0.1$ and all the other simulations parameters are the same as described previously. In order to compare the kinetic simulations with theory, the generalized expressions for the collisional momentum exchange in Appendix A are employed. All terms on the left-hand-side of Eq. (14) are computed directly from the PIC simulation, while the friction and thermal forces are estimated from Eqns. (A1)-(A2) using the moments and fields within the simulation. The various terms are averaged in time over the interval $t\nu_{ei}^o = 5 \rightarrow 10$ (corresponding to $t\Omega_{io} = 1.25 \rightarrow 2.5$). At the end of this interval, the observed electron heating in center of the layer is $\Delta T_e/T_o = 0.092$, 0.12 and 0.13 for these three cases. These observed values are somewhat larger than the simple estimate in Eq. (20) which gives $\Delta T_e/T_o \approx 0.085$ using the parallel resistivity $\hat{\eta}_{\|o}$. Since the ratio $B_o/B*$ in Eq. (23) can be much larger for weak guide field, the thermal force is expected to be more significant. This is confirmed in Fig. 4 where the dominant terms in the y-force balance are illustrated for these three cases. Electron inertia and $\nabla \cdot \mathbf{P}_e$ are again completely negligible, and the non-ideal electric field is approximately balanced by the combination of friction and thermal forces. It is important to note that the thermal force arising from $\nabla T_e \times \mathbf{B}$ is always in the opposite direction as the friction force, and thus acts to maintain the current. The thermal force is zero at $z \rightarrow 0$ where the temperature gradient vanishes, but can be as large as $\sim 30\%$ of E_y in the edge region where the temperature gradient is large.

The discrepancy between the kinetic simulation and transport theory is somewhat larger in Fig. 4 than for the strong guide field results in Fig. 3. In our view, this is probably due to limitations in the theory rather than a problem with the simulations. Since the collision algorithm conserves momentum exactly, the red line in Figs. 3-4 corresponds to the actual momentum exchange $\mathbf{R_e}$ in the simulation. The theory may differ from the simulation results for a number of reasons. First, the estimated uncertainty in these expressions [27] is considerably larger $\sim 10 - 20\%$ in the regime $\nu_{ei} \sim \Omega_e$ encountered at weak guide field. In addition, classical transport theory does not properly include effects arising from the inhomogeneity in the magnetic field, such as electron ∇B drifts. In the neutral sheet limit, electrons undergo a variety of complicated meandering electron orbits in the central region of the layer. Despite these uncertainties, the maximum deviation for the neutral sheet limit is only $\sim 10\%$ in Fig. 4. This level of uncertainty is not significant for interpreting the reconnection simulations. It should be noted, that recent laboratory experiments have measured both the parallel and perpendicular resistivity in a reconnecting current sheet [36, 37], under the assumption that the thermal force is negligible. The reported results are within $\sim 30\%$ of the theoretical predictions for the parallel and perpendicular resistivities.

TABLE I: Summary of simulation parameters: initial perpendicular resistivity $\hat{\eta}_{\perp o}$, system size L_x, number of computational cells N_x, initial Lundquist number $S_o \equiv 4\pi V_A L_{sp}/(\eta_{\perp o} c^2)$, critical resistivity $\hat{\eta}_c$ required for $\delta_{sp} \approx d_i$, and electron heating T_c/T_o needed to reach $\hat{\eta}_c$. The system size in the transverse direction is $L_z = 50d_i$ (800 cells), the time step is $\Delta t\Omega_{ce} = 0.13$ and there are 2000 computational particles per cell.

$\hat{\eta}_{\perp o}$	L_x/d_i	N_x	S_o	$\hat{\eta}_c$	T_c/T_o
0	100	1600	∞	-	-
	200	3200	∞	-	-
0.04	100	1600	625	0.04	1
	200	3200	1250	0.02	1.58
0.1	100	1600	250	0.04	1.84
	200	3200	500	0.02	2.92
0.2	100	1600	125	0.04	2.92
	200	3200	250	0.02	4.64

IV. RECONNECTION SIMULATIONS

In this initial study, we consider the transition between collisional and collisionless reconnection within neutral sheet geometry. Two-fluid simulations and theory [12–14] predict a transition from Sweet-Parker (SP) to fast reconnection when the half-thickness δ_{sp} of the resistive layer falls below the ion inertial length d_i. Within the SP regime, the layer half-thickness is $\delta_{sp}/L_{sp} \approx S^{-1/2}$ where $S \equiv 4\pi V_A L_{sp}/\eta c^2$ is the Lundquist number , L_{sp} is the half-length the SP current layer and V_A is the Alfvén speed based on the upstream plasma conditions. For periodic boundary conditions, fluid simulations [13] indicate that half-length of the SP layer is roughly $L_{sp} \approx L_x/4$, where L_x is the domain size in the x-direction. Taking this into account, the transition condition $\delta_{sp} \leq d_i$ may be re-expressed as

$$\hat{\eta} \leq \frac{d_i}{L} \approx \frac{4d_i}{L_x} \equiv \hat{\eta}_c \,, \qquad (25)$$

where $\hat{\eta}_c$ is the critical value of the resistivity where the transition is expected to occur.

In the present kinetic study, there are a number uncertainties to keep in mind regarding this transition condition (25). Fluid models of reconnection typically treat resistivity as spatially uniform without regard to the orientation of the magnetic field, while the thermal force is neglected completely. In the collisional kinetic simulations,

significant variations in resistivity across the layer are unavoidable if the Coulomb collisions are treated physically, since Ohmic heating always leads to order unity variations in T_e. In addition, the orientation of the magnetic field and the local magnetization parameter Ω_e/ν_{ei} vary across the layer, introducing a factor of ~ 2 uncertainty in which resistivity to employ in Eq. (25). In the previous section, it was demonstrated that the unmagnetized resistivity $\eta_{sp} = \eta_{\parallel}$ is recovered in the central region defined by Eq. (24), while $\eta_{\perp}$ applies to the bulk of the current layer. Furthermore, it appears that the perpendicular resistivity is setting the overall width of the resistive layer when the simulations are in a SP configuration. Thus we will employ the perpendicular coefficient when discussing the various simulations. The dimensionless parameter $\hat{\eta}_{\perp o}$ characterizes the initial perpendicular resistivity everywhere, since the initial temperature T_o is uniform. As discussed in Sec. III C, Ohmic heating within the current layer causes the actual resistivity to vary in space and time according to Eq. (18). Based on these considerations, SP reconnection is expected when $\hat{\eta}_{\perp} > \hat{\eta}_c$ while a transition to fast reconnection is expected when electrons are heated to a critical temperature T_c such that $\hat{\eta} \leq \hat{\eta}_c$.

To examine this transition, we consider the Harris sheet initial condition with zero guide field $B_y = 0$ and with equal temperature for both ions and electrons $T_e = T_i = T_o$. The mass ratio is $m_i/m_e = 40$ and the initial current sheet thickness is $\lambda = d_i$. In order to accommodate the larger systems, it was necessary to choose $\omega_{pe}/\Omega_{ce} = 2$ which implies $v_{the}/c \approx 0.35$. A uniform nondrifting background population is included with density $n_b = 0.3n_o$ and the same temperature. Holding these initial current sheet parameters fixed, the collisionality is systematically varied using the same approach and normalizations described in Sec. III C. The range of initial collisionality and system size are summarized in Table I, along with the number of computational cells, the initial Lundquist number S_o, the critical value of resistivity $\hat{\eta}_c$ from Eq. (25) and the electron heating required to produce this resistivity. To initiate reconnection in a controlled manner, a magnetic perturbation of the form

$$\delta B_x = -\frac{\delta B}{2}\left(\frac{L_x}{L_z}\right)\cos\left[\frac{2\pi(x-0.5L_x)}{L_x}\right]\sin\left(\frac{\pi z}{L_z}\right),$$
$$\delta B_z = \delta B \sin\left[\frac{2\pi(x-0.5L_x)}{L_x}\right]\cos\left(\frac{\pi z}{L_z}\right),$$

is imposed with $\delta B = 0.025B_o$ for all cases. The reconnection rate E_R is calculated from

$$E_R = \frac{1}{BV_A}\left\langle\frac{\partial\psi}{\partial t}\right\rangle, \tag{26}$$

where $\psi = \max(A_y) - \min(A_y)$ along $z = 0$, A_y is the y-component of the vector potential, B and V_A are evaluated at $10d_i$ upstream of the dominant x-point and $\langle\ \rangle$ represents a time average over $\Delta t\Omega_{io} = \pm 3$ in order to eliminate high frequency noise.

In the collisional simulations, there is an initial period of rapid electron heating consistent with Eq. (20) which causes the initial Harris sheet to expand outwards. As the reconnections flow develop within the SP regime, the ions and electrons come into thermal equilibrium on a time scale $\tau_{eq}\Omega_{io} \sim 1/\hat{\eta}_{\perp}$, after which the central temperature is largely determined by the pressure balance condition (22) across the layer. Assuming the upstream conditions do not change significantly during this initial phase, the maximum central temperature is limited by $T_e/T_o < (n_o + n_b)/n_c$ where n_c is the time evolving central density in the layer. In this study, typical values are in the range $n_c/n_o \sim 0.5 - 0.8$ during collisional SP reconnection which implies $T_e/T_o \sim 1.6 - 2.6$.

To examine the transition condition, the time evolution for the $L_x = 100d_i$ simulations is illustrated in Fig. 5. As shown in the top panel, the reconnection rate for the most collisional case $\hat{\eta}_{\perp o} = 0.2$ (black curves) remains slow throughout the simulation, while the rates at lower collisionality are eventually comparable to the collisionless limit (red curves). This result is in good agreement with the predictions in Table I, since the electron temperature reaches a maximum of $T_e/T_o \sim 2.2$ for the $\hat{\eta}_{\perp o} = 0.2$ case as shown in the second panel, while the required transition temperature is $T_e/T_o \sim 2.9$. As a consequence, the time evolving resistivity shown in the third panel, remains above the critical value of $\hat{\eta}_c \approx 0.04$. In addition, the current sheet half-thickness δ_{min} remains somewhat larger than the local ion skin depth d_{i*} computed using the actual density within the layer, as illustrated in the bottom panel. In contrast, the reconnection rate for the case with initial resistivity $\hat{\eta}_{\perp o} = 0.1$ (blue curves) remains in a slow regime until approximately $t\Omega_{io} = 75$, after which the rate increases to approximately the same range as the collisionless limit. As illustrated by the dashed line, the transition electron temperature and resistivity are in good agreement with the expected values in Table I. After the transition, the three simulations in the fast regime develop electron scale current layers with $\delta_{min} \approx (1.8 - 2.4)d_{e*}$, where the electron skin depth d_{e*} is based on actual layer density.

From the above discussion, the $\hat{\eta}_{\perp o} = 0.1$ simulation is a clear example illustrating the transition between the collisional SP and kinetic regimes. To better illustrate the structure of the layer before and after this transition, the contours of the current density J_y are shown in left panels of Fig. 6. At early time $t\Omega_{io} = 50$, the current layer is elongated as expected for the SP regime, while at later time $t\Omega_{io} = 120$ the current sheet is much shorter resulting in a faster rate. The out-of-plane collisional momentum exchange across each current sheet is illustrated on the right panels. The red curves are evaluated directly from the simulation by summing the left hand side of Eq. (14). Since the collision algorithm conserves momentum exactly, this should correspond to the true collisional momentum exchange R_e within the simulation. The thermal force (blue) and friction force (green) are estimated using the generalized Braginskii

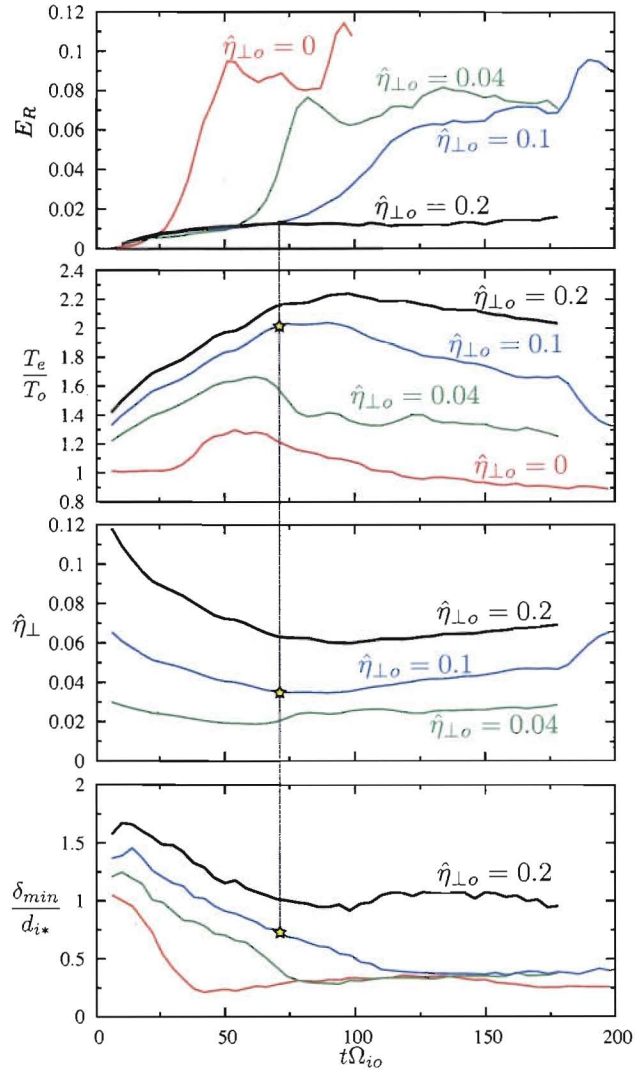

FIG. 5: Time evolution for the $L_x = 100d_i$ simulations in Table I showing the reconnection rate E_R, the electron temperature T_e in the center of the layer, the perpendicular resistivity $\hat{\eta}_\perp$ implied by Eq. (18) and the minimum half-thickness δ_{min} normalized to the ion inertial length d_{i*} based on the time evolving central density. The vertical dashed line highlights the transition time for the $\hat{\eta}_{\perp o} = 0.1$ simulation.

expressions in Appendix A, evaluated with the actual moments and fields within the kinetic simulation. For the SP regime in the top panel, the sum of these two terms (black) is good agreement near the center and in the outer region $|z| > d_i$, while the theoretical expression is $\sim 20\%$ larger along the edge of the layer, where electron ∇B drifts are significant. This implies that the actual resistivity within the simulation follows the basic theoretical expectations (and uncertainties) discussed previously. When the reconnection layers are in a resistive SP regime, the central resistivity is known to within an uncertainty of $\sim 5\%$, with somewhat larger uncertainties $\sim 20\%$ in regions with large ∇B. In contrast, the lower right panel illustrates this same comparison for the fast regime in which the current layer has collapsed to the electron scale. In this limit, the discrepancy between transport theory and the collisional kinetic simulations is considerably larger $\sim 40\%$. However, some of the basic assumptions of transport theory are clearly violated in this regime, as discussed below.

The structural transition shown in Fig. 6 is accompanied by fundamental changes in the mechanism responsible for breaking the frozen-in condition. To elucidate these changes, the various terms in the out-of-plane electron momentum equation are shown in Fig. 7 for the same spatial regions highlighted by the white boxes in Fig. 6. For the SP configuration at early time $t\Omega_{io} = 50$, approximately 90% of the non-ideal electric field is balanced by collisional momentum exchange, while the divergence of the electron pressure tensor accounts for $\sim 10\%$ in the central region and the inertial term is completely negligible. At this time, the ratio of the reconnection electric field to the runaway limit is approximately $E_y/E_{cr} \approx 0.18$ near the x-point. At later time $t\Omega_{io} = 120$ after the transition, this ratio is approximately $E_y/E_{cr} \approx 1.2$. In this runaway regime shown in the lower panel of Fig. 7, collisional momentum exchange is increasingly ineffective and transport theory breaks down. The electron distribution in this layer has strong non-Maxwellian features, so using $T_e \approx \mathrm{Tr}(\mathbf{P}_e)/(3n_e)$ to estimate the theoretical $\hat{\eta}_\perp$ in Eq. (18) is clearly questionable. Within the electron layer, nearly $\sim 60\%$ of the non-ideal electric field is balanced by $\nabla \cdot \mathbf{P}_e$ while the remaining portion is due to collisional momentum exchange $\mathbf{R}_e$. The fraction of the field supported by $\nabla \cdot \mathbf{P}_e$ is clearly a strong function of E_y/E_{cr}, and this functional relationship will be detailed in a future publication. Finally, it should be noted that immediately upstream of the electron layer, the inertial term is significant with sign opposite to $\nabla \cdot \mathbf{P}_e$. Likewise, electron inertia plays a role in the downstream region (not shown) but $\nabla \cdot \mathbf{P}_e$ remains dominant.

As illustrated in the top panel of Fig. 8, there is a weak $B_y/B_o \sim 0.05$ elongated quadrupole structure when the reconnection layer is still in the SP configuration. Presumably, this is due a weak decoupling of the electron and ion outflows. This feature is also consistent with the weak $\nabla \cdot \mathbf{P}_e$ term present in the top panel of Fig. 7. However, as the intense electron scale layer forms (see bottom panel of Fig. 6) there is a factor of $\sim 3-4$ enhancement in the magnitude of the quadrupole field as illustrated in the bottom panel of Fig. 8.

Many of the results illustrated in Figs. 6-8 are consistent with expectations from two-fluid simulations [12–14]. The existence of the scale separation in the inflow direction and the resulting quadrupole field are both well understood features of magnetic reconnection in collisionless neutral sheet geometry. However, the physics responsible for controlling the ultimate length of the electron and ion current layers remains controversial and poorly understood. In the collisionless limit, recent large-scale kinetic simulations have demonstrated that the electron

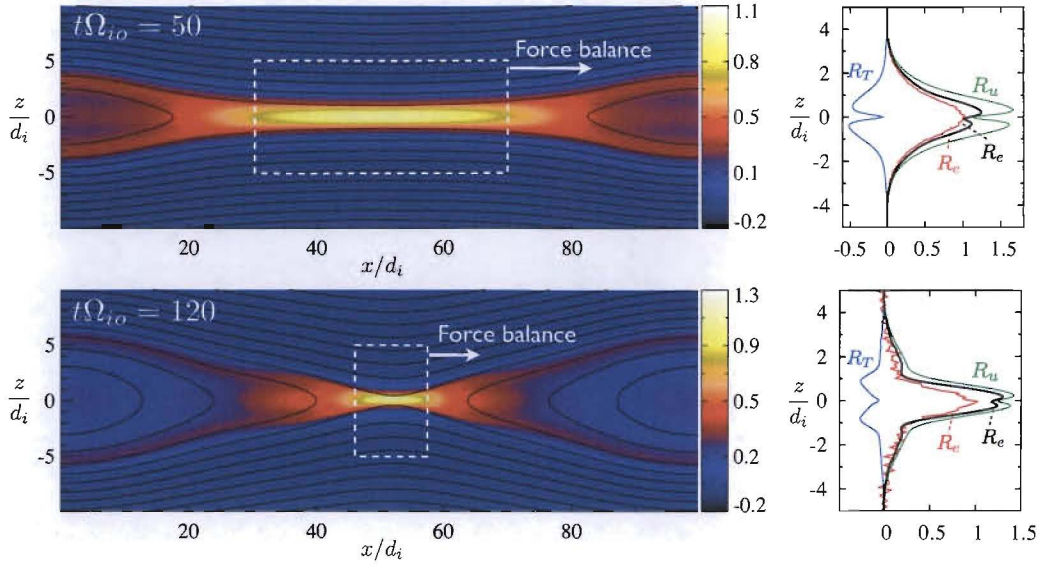

FIG. 6: Contours of current density J_y for the $L_x = 100d_i$ simulation with initial resistivity $\hat{\eta}_{\perp o} = 0.1$ for the two simulation times indicated. Black lines are the flux surfaces. At early time in the top panel, the reconnection layer is in a Sweet-Parker configuration. Due to Ohmic electron heating, the resistivity falls below the critical threshold (see Fig. 5), and the layer contracts dramatically as illustrated in the bottom panel. The right panels compare the out-of-plane collisional momentum exchange with transport theory as described in the text. Curves are normalized such that $R_e = 1$ at the center of the layer.

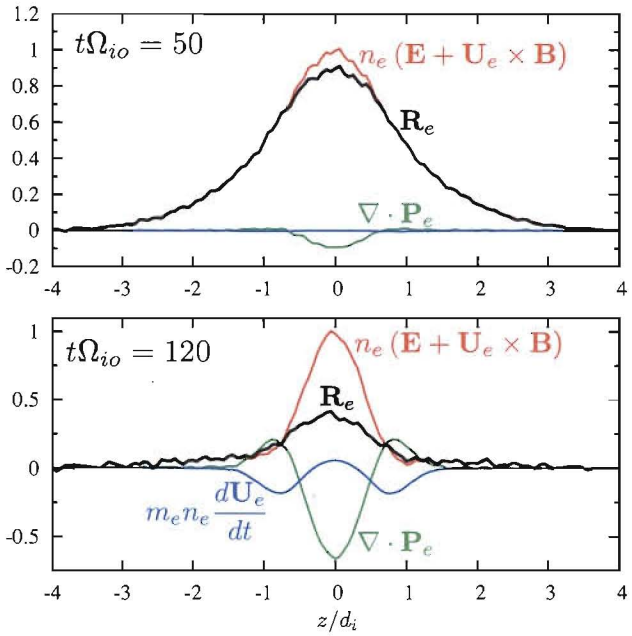

FIG. 7: Electron momentum balance in the y-direction across the diffusion region at early time (top) when the layer is in the SP regime and later time (bottom) after the transition to the kinetic regime. The non-ideal electric field (red), electron inertia (blue) and pressure tensor (green) are computed directly from the simulation. These results are for the $L_x = 100$ case with $\hat{\eta}_{\perp o} = 0.1$ and correspond to the same regions highlighted in Fig. 6 with white boxes. The terms in Eq. (14) are normalized by the electric field E_y near the x-point.

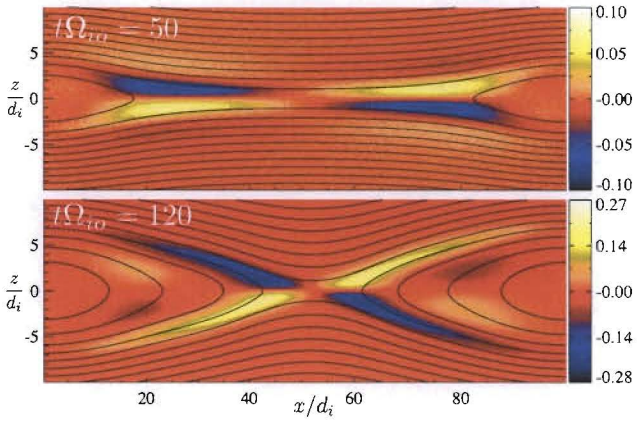

FIG. 8: Structure of the quadrupole magnetic field B_y (normalized to B_o) for the same two simulation times illustrated in Figs. 6-7. Black lines are flux surfaces.

layer can form highly elongated current sheets [22–25] that are completely at odds with two-fluid simulations. While the electron layer shown in the bottom panel of Fig. 6 is relatively short immediately after the transition, the full length $\sim 10d_i \approx 63d_e$ is still dramatically longer than reported in two-fluid simulations. Furthermore, over longer time scales the electron layer is observed to elongate in the outward direction leading to secondary island formation in a manner very similar to previous collisionless simulations [22, 23, 25]. In order to illustrate the structure of the layer prior to the onset of secondary islands, Fig. 9 compares the electron flow velocity, quadrupole field and ion outflow between

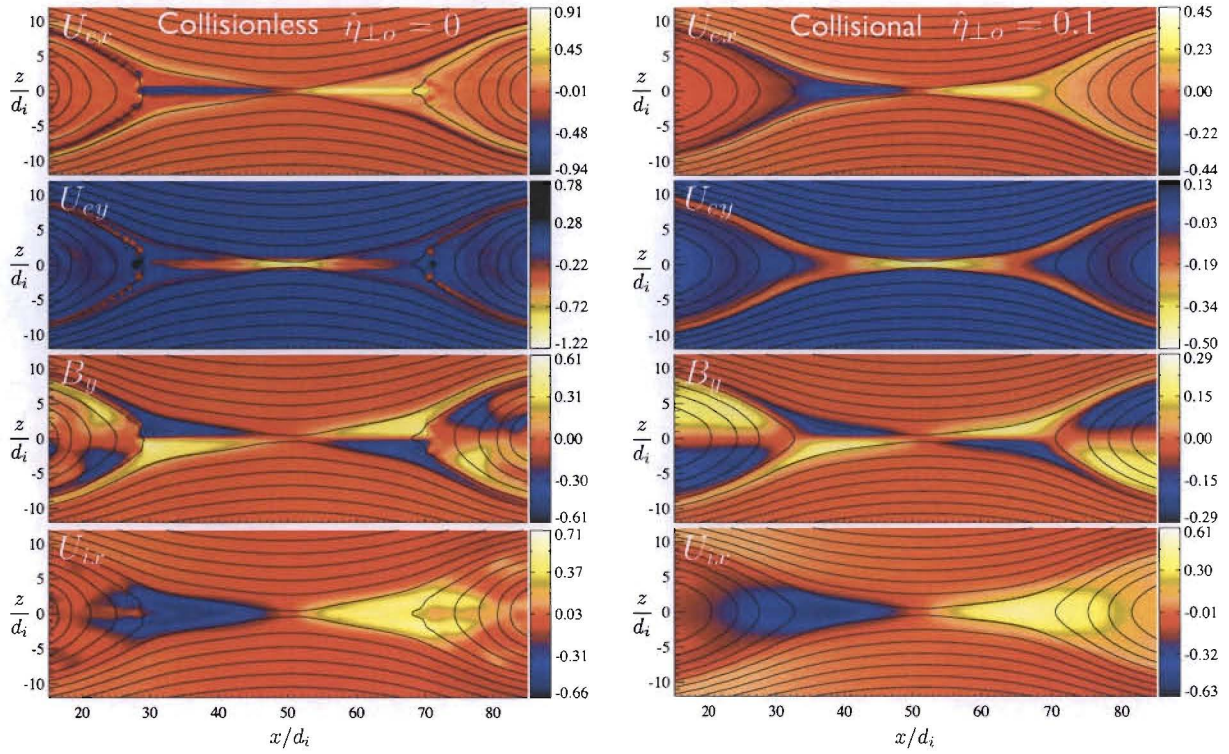

FIG. 9: Comparison between a collisionless simulation (left panels) at time $t\Omega_{io} = 100$ and a collisional simulation $\hat{\eta}_{\perp o} = 0.1$ in the fast regime at time $t\Omega_{io} = 160$ (right panels). Shown are the electron outflow velocity U_{ex}, the electron out-of-plane velocity U_{ey}, the quadrupole B_y/B_o structure and the ion outflow U_{ix}. The system size is $L_x = 100$ for both cases and the times were chosen to illustrate the structure just before the onset of plasmoid formation within the electron layer. Electron velocities are normalized to the initial thermal speed and the ion outflow is normalized by the upstream Alfvén speed.

this simulation ($L_x = 100d_i$ and $\hat{\eta}_{\perp o} = 0.1$) and the corresponding collisionless run. In both cases, the simulation times were selected to correspond to the longest electron layer before the onset of plasmoids. In the collisionless limit, the electron outflow jets remain highly collimated out to distance of $\sim 20d_i$ from the x-line, while in the semi-collisional simulation the jets begin to diverge sooner and are broadened by $\sim 50\%$ due to the collisions. The thickness of the electron layer near the x-point is $\sim 30\%$ broader and the peak flow is reduced by $\sim 50\%$. As a result, the magnitude of the quadrupole field shown in the third panel is also reduced by $\sim 50\%$. However, both the ion outflow (bottom panel) and the reconnection rate (see Fig. 5) are quite close.

Over longer simulation times, both the collisionless and semi-collisional simulations form secondary magnetic islands within the electron layer. The time evolution of the electron layer for this same case with initial resistivity $\hat{\eta}_{\perp o} = 0.1$ is illustrated in Fig. 10. The formation of a plasmoid at $t\Omega_{io} \approx 180$ is accompanied by an increase in the reconnection rate shown in the top panel of Fig. 5. Presumably, this is due to the shorter electron layer as shown in the last two panels of Fig. 10. This result implies that the dynamics of the electron layer can influence the reconnection rate in manner similar to recent collisionless simulations [22, 23, 25]. In this particular simulation, only one plasmoid is formed and ejected from the electron layer. After this time, the system has saturated due to the periodic boundary conditions. In order to examine the influence of plasmoids over longer time scales, it will be necessary to employ open boundary conditions [22] or to use much larger system sizes.

In order to examine the transition physics in somewhat larger systems, we next consider the $L_x = 200d_i$ simulations in Table I. For this system size, the critical resistivity $\hat{\eta}_c \approx 0.02$ is below the initial resistivity for all three collisional cases in Table I. The time evolution of the reconnection rate, electron temperature, resistivity and minimum layer thickness are given in Fig. 11. Again, there is a clear distinction in the reconnection rate for the most resistive simulation $\hat{\eta}_{\perp o} = 0.2$ in comparison to the other three runs. As indicated by the vertical dashed line, the simulation with initial resistivity $\hat{\eta}_{\perp o} = 0.04$ shows an abrupt transition to faster reconnection when the electron temperature and resistivity approach the critical value. Despite this agreement with Eq. (25), closer inspection reveals the growth of 3 secondary islands (or plasmoids) within the SP layer during $t\Omega_{io} \approx 40 - 70$. This same basic scenario was also observed in the simulation with initial resistivity $\hat{\eta}_{\perp o} = 0.1$. In this case, the transition to faster reconnection occurs when the resistivity $\hat{\eta}_{\perp} \approx 0.035$ is significantly above the

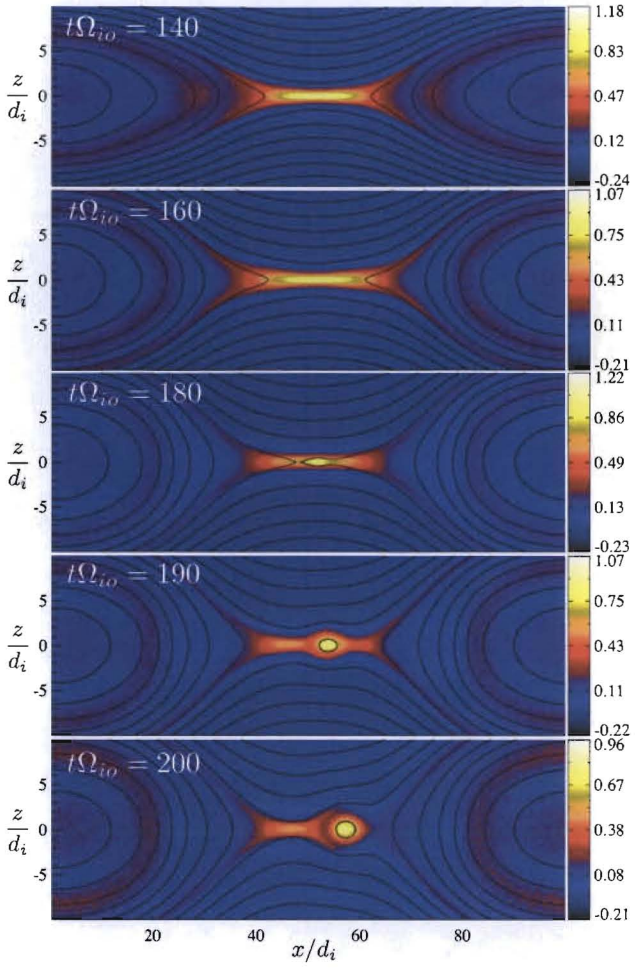

FIG. 10: Time evolution of the current density J_y (normalized to J_o) after the transition to fast reconnection for the $L_x = 100d_i$ simulation with initial resistivity $\hat{\eta}_{\perp o} = 0.1$. This is the same case discussed in Figs. 6-8. Black lines represent the flux surfaces.

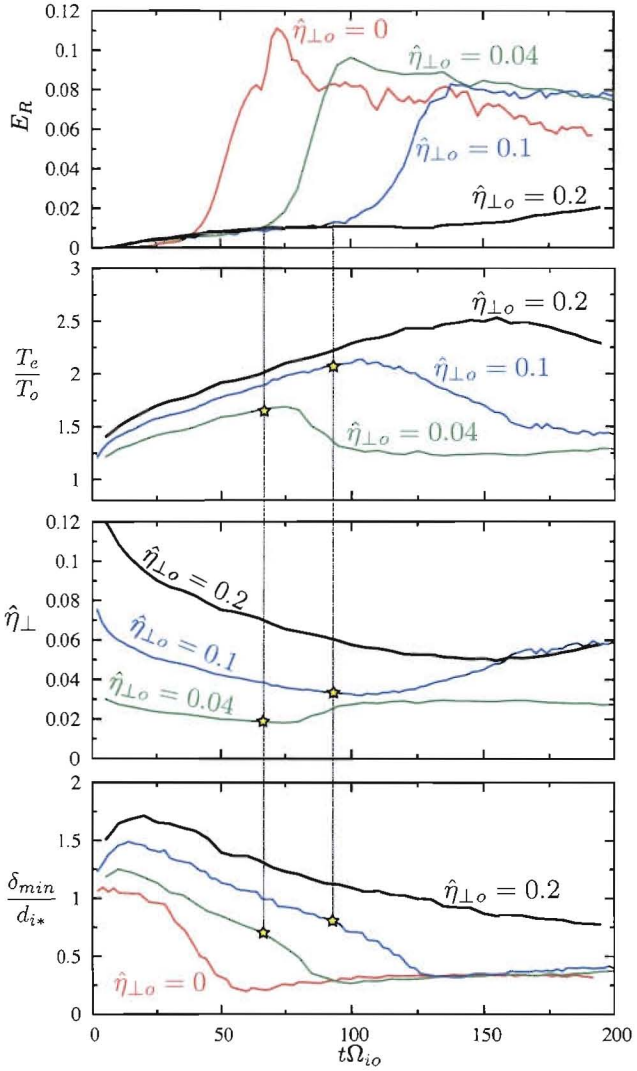

FIG. 11: Time evolution for the $L_x = 200d_i$ simulations in Table I shown the the reconnection rate E_R, the electron temperature T_e in the center of the layer, the perpendicular resistivity $\hat{\eta}_\perp$ implied by Eq. (18) and the minimum half-thickness δ_{min} normalized to the local ion inertial length d_{i*} based on the time evolving central density. The vertical dashed lines highlight the transition conditions for the $\hat{\eta}_{\perp o} = 0.04$ and $\hat{\eta}_{\perp o} = 0.1$ simulations.

expected transition value. While the smaller $L_x = 100d_i$ simulation in Figs. 6-8 remains in a single x-line configuration throughout the transition, the longer SP layer in the $L_x = 200d_i$ simulation is unstable to plasmoid formation as illustrated in Fig. 12. During the initial phase, the reconnection layer features the classic Sweet-Parker structure. However, a magnetic island is observed to form near time $t\Omega_{io} \approx 100$ leading to the formation of two electron scale layers by $t\Omega_{io} \approx 130$, as illustrated in the bottom panel of Fig. 12. The measured layer thickness δ_{min} in the bottom panel of Fig. 11 corresponds to the minimum scale across the entire simulation domain in the x-direction. While at early time $t\Omega_{io} < 70$ this measurement accurately reflects the thickness of the SP layer, at later times this corresponds to the thickness of the current sheet between the magnetic islands. This feature in the evolution allows the onset to fast reconnection to occur sooner than expected from the simple criteria $\delta_{sp} \approx d_i$, which is based on the assumption that the Sweet-Parker solution is structurally stable. As mentioned previously, recent linear theory with resistive MHD has predicted that SP layers are unstable [10] to a tearing-like instability at high Lundquist number with a super-Alfvénic growth rate. However, the asymptotic theory assumes highly elongated layers and thus cannot predicted the critical Lunquist number corresponding to the onset of instability. The simulation shown in Fig. 12 corresponds to a Lundquist number of $S \approx 1400$ at the time when magnetic islands begin to form.

The two simulations in Table I with high initial resistivity $\hat{\eta}_{\perp o} = 0.2$ remain well above the expected two-fluid transition condition and the resulting reconnection rates

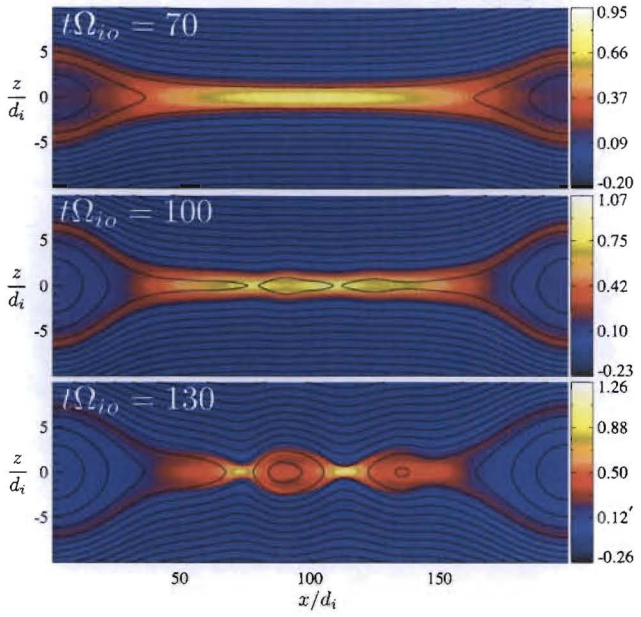

FIG. 12: Time evolution of the current density J_y for the $L_x = 200d_i$ simulation with initial resistivity $\hat{\eta}_{\perp o} = 0.1$. The transition away from Sweet-Parker (top panel) involves the formation of magnetic islands in the resistive layer. The black lines are the magnetic flux surfaces and the current density is normalized to the initial peak value J_o.

in Figs. 5 and 11 are a factor of 5-8 smaller than the other simulations in the fast regime. However, the crucial point is not the precise numerical value of these rates but rather the scaling of the rate with system size and dissipation. Although in the top panel of Fig. 5 there may be a weak dependence on resistivity for the simulations in the fast regime, the larger simulations in Fig. 11 show very similar rates for the simulations in the fast regime. Furthermore, these rates are slightly larger than the corresponding smaller runs, indicating a weakly *increasing* dependence on the system size. Although the variation in system size is only a factor of two, these initial scaling results are clearly favorable for explaining fast reconnection in large systems.

Regarding the two most resistive simulations in this initial study, it is important to examine whether the observed rates follow the expected SP scaling. Although this question is complicated by the time dependent nature of the resistivity within the layer, Figs. 5 and 11 demonstrate that the time evolution of the electron heating and resulting resistivity are actually quite close for the two $\hat{\eta}_{\perp o} = 0.2$ simulations. Thus the SP scaling implies the $L_x = 200d_i$ simulations should be slower than the $L_x = 100d_i$ case by a factor of $\sqrt{2}$. In order to test this scaling prediction, the reconnection rate for these two cases are compared in Fig. 13. To facilitate the comparison, the $L_x = 100d_i$ result is also re-plotted with the $1/\sqrt{2}$ scaling factor (see dashed red line). At early time $t\Omega_{io} < 70$, the rate in the larger case is in good agreement with the SP scaling, while at later time

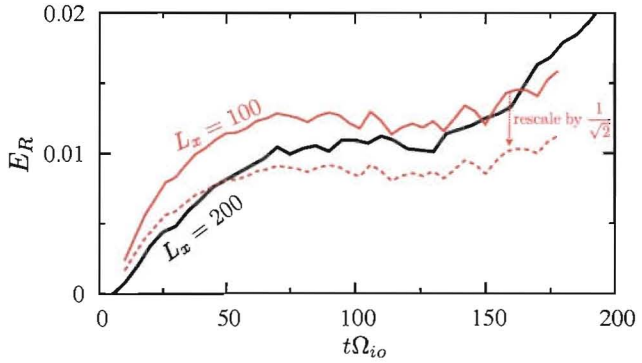

FIG. 13: Comparison of the reconnection rate for the two most resistive ($\hat{\eta}_{\perp o} = 0.2$) simulations in Table I with system size $L_x = 100d_i$ (red) and $L_x = 200d_i$ (black). In order to test the Sweet-Parker scaling, the reconnection rate for the $L_x = 100d_i$ simulation is rescaled by $1/\sqrt{2}$ (dashed red).

$t\Omega_{io} > 150$ the rate in the larger run overtakes the smaller case. Closer inspection reveals this breakdown in the SP scaling is accompanied by the formation of a magnetic island within the layer in a manner very similar to Fig. 12. It should be emphasized that the minimum resistivity $\hat{\eta}_\perp \gtrsim 0.05$ in this simulation is considerably larger than the expected critical value $\hat{\eta}_c = 0.02$ throughout the simulation (see Fig. 11). However, the formation of magnetic islands within the SP layer gives rise to current enhancements near the new x-points. As a result, the scale of these current structures falls below an ion inertial length at $t\Omega_{io} \approx 120$ as illustrated in the bottom panel of Fig. 11. Thus the larger $L_x = 200d_i$ simulation forms current structures that are significantly narrower than the $L_x = 100d_i$ simulation (see Fig. 5) due to the secondary reconnection instability within the layer. Since the magnetic island forms at rather modest Lundquist number $S \approx 850$, this suggests that SP reconnection may be rather fragile in most real applications.

V. SUMMARY

The inclusion of a Fokker-Planck collision operator within fully kinetic simulations is a powerful first-principles technique to examine many basic questions regarding the transition between collisional and collisionless regimes. The initial efforts described in this manuscript have laid the necessary groundwork in order to confidently perform and interpret these simulations for basic studies of magnetic reconnection. In particular, it has been established that the collision algorithm is in excellent agreement with some of the most fundamental predictions from classical transport theory, including the slowing down and diffusion of a test beam and the Spitzer resistivity for an unmagentized plasma.

For reconnection problems, it is essential to understand the detailed form of the collisional momentum exchange in a magnetized plasma. This was accomplished by exam-

ining the collisional decay of a current layer for a range of guide fields. In the limit of strong guide field, the measured friction force is within $\sim 4\%$ of transport theory while the thermal electric force is negligibly small for the cases considered. For the neutral sheet limit, the thermal force is a substantial fraction $\sim 30\%$ of the non-ideal electric field on the edge of the current layer. Furthermore, the thermal force $\nabla T_e \times \mathbf{B}$ is always in the opposite direction of the friction force and thus acts to maintain the current. In the neutral sheet limit, detailed comparisons with transport theory reveals some modest discrepancies. In the central region of the layer defined by $\Omega_e < \nu_{ei}$, the resistivity is within $\sim 5\%$ of the unmagnetized Spizter coefficient, while in the strongly magnetized $\Omega_e \gg \nu_{ei}$ outer region the resistivity increases by a factor of ~ 2 to recover the perpendicular result. In edge region of the layer, differences with transport theory are larger $\sim 10\%$, but the theory does not include the strong electron ∇B drifts or the complicated electron meandering motion.

These benchmarks have established that Coulomb collisions can be introduced within the fully kinetic simulations in a controlled fashion so that the electrical resistivity is well determined. It should be emphasized that a physical treatment of Coulomb collisions includes a range of complexities not normally treated within fluid simulations of reconnection. In particular, electron Ohmic heating in SP regimes is always of order unity and thus strong spatial and temporal variations in the resistivity are unavoidable. Furthermore, the electron heating across the current layer leads to a substantial thermoelectric contribution to the collisional momentum exchange in the edge region of a neutral sheet. In strongly magnetized regions, the resistivity is a factor of ~ 2 lower along magnetic field lines than across and in weakly magnetized regions the resistivity is a function of Ω_e/ν_{ei}.

Although there are a range of reconnection problems that may benefit from this first-principles approach, this initial study focused on the transition between collisional and collisionless reconnection in neutral sheet geometry. Despite the complications discussed above, the collisional kinetic simulations are in agreement with some key predictions from fluid theory. In particular, the classic SP solution is recovered for the two most resistive kinetic simulations in the present study. For the $L_x = 100d_i$ simulation with $\hat{\eta}_{\perp o} = 0.2$, the Ohmic heating within the layer never reaches the expected threshold value and the steady reconnection rate is consistent with compressible resistive MHD using the same parameters.

For the $L_x = 100d_i$ simulation with initial resistivity $\hat{\eta}_{\perp o} = 0.1$, the electron Ohmic heating within the SP layer gives rise to a clear transition to faster reconnection when the thickness of the resistive layer falls below the ion inertial length $\delta_{sp} \lesssim d_i$. Associated with this transition are a number of distinct structural changes: (1) the thickness of the diffusion region current sheet collapses to the electron scale, (2) the length of this electron sheet is much shorter than the SP layer and (3) the out-of-plane quadrupole field is greatly enhanced. Many of these features are consistent with previous expectations from two-fluid theory and simulations [12–14]. However, other aspects of the transition are problematic to describe with fluid theory. For example, after the transition to fast reconnection the reconnection electric field is above the runaway limit where transport theory clearly breaks down (i.e. $\eta\mathbf{J}$ in Ohm's law has no justification) and collisionless processes must take over. In this regime, it is not clear how to correctly model the non-ideal electron terms within fluid theory. However, the first-principles kinetic approach in this study is valid for arbitrary collisionality, and these initial simulations have demonstrated that the non-ideal electric field is balanced predominantly by $\nabla \cdot \mathbf{P}_e$ when the reconnection electric field exceeds the runaway limit $E_y \gtrsim E_{cr}$. The fraction of E_y balanced by $\nabla \cdot \mathbf{P}_e$ is clearly a strong function of E_y/E_{cr}, and this relationship will be detailed in a future publication. Within fluid closures, the off-diagonal terms in $\nabla \cdot \mathbf{P}_e$ corresponds to a viscosity, but it is presently unclear whether any existing theory is capable of accurately describing these terms within the weakly collisional electron-scale layers observed in the present simulations.

In the collisionless limit, the basic $\nabla \cdot \mathbf{P}_e$ mechanism for breaking the frozen-in condition has been discussed extensively [20, 38], but it was only recently demonstrated to play a central role in controlling the length of the electron layers [23]. This important issue brings us to a fundamental discrepancy between the kinetic simulations and the fluid models. In the present study, the full length of electron layer after the transition $\sim 10d_i \approx 63d_e$ is much longer then reported $\sim 10d_e$ in two-fluid and hybrid simulations [16]. Furthermore, as the collisional kinetic simulations proceed in the fast regime, the electron layer expands further in the outward direction and becomes unstable to the formation of secondary islands in a manner similar to recent collisionless kinetic simulations [22, 23, 25]. These results indicate that the electron layer plays an important role in determining the time evolution of the reconnection rate. Furthermore, these results clearly demonstrate that the basic structure and dynamical evolution of the electron diffusion region is dramatically different than predicted by two-fluid and hybrid descriptions. Since Eq. (1) is the ultimate starting point for all reduced fluid descriptions, the computational approach in this manuscript has great potential to help resolve these fundamental issues.

Regarding the transition between collisional Sweet-Parker dynamics and the faster kinetic regime, the smaller simulations in this study are in good agreement with the condition $\delta_{sp} \lesssim d_i$ expected from two-fluid theory [12–14]. However, it should be emphasized that this condition assumes that SP layers are structurally stable at high Lundqust number. The larger simulations in this initial study have already demonstrated that the SP current layers are unstable to a secondary reconnection instability at rather modest Lundquist numbers $S \sim 1000$. In the $L_x = 200$ simulation with $\hat{\eta}_{\perp o} = 0.2$, the growth of magnetic islands lead to significant departure from the

SP scaling, while in the less resistive case $\hat{\eta}_{\perp o} = 0.1$ the magnetic islands lead to the onset of fast reconnection sooner than expected based on the $\delta_{sp} \approx d_i$ condition. In even larger systems, it remains unclear whether the onset of two-fluid physics or the stability of the SP layer will dominate the basic transition to faster reconnection.

Even within the context of resistive MHD, the stability of SP layers and the influence on the reconnection rate remains an outstanding issue. The recent linear theory on this problem [10] represents an important step forward, but these results cannot predict the influence on the rate nor reveal the critical Lundquist number beyond which SP solutions break down. In future studies with the collisional kinetic simulations, it is important to consider a wider range of system sizes and Lundquist numbers in order to examine what range of parameters the SP solution is valid and whether the transition away from this solution is governed by the onset of two-fluid physics or by the structure stability of the elongated SP current layers. Many of these basic questions can and should be addressed within the context of fluid and simulations. Differences may well occur due to the physical treatment of Coulomb collisions, and it is important to understand this as well. Finally, the formation of magnetic islands within an elongated SP layer may push the dynamics into the kinetic regime and the computational approach in this manuscript is uniquely capable of the describing this entire transition scenario.

APPENDIX A: GENERAL FORM OF COLLISIONAL MOMENTUM EXCHANGE

The expressions for the friction and thermal force given in Eqns. (15)-(16) are valid in the strongly magnetized limit $\nu_{ei} \ll \Omega_e$. For arbitrary magnetic field, these terms are considerably more complicated [27]. The general form of the friction force is

$$\mathbf{R}_u = e n_e \left(\eta_{\parallel} \mathbf{J}_{\parallel} + \eta_{\perp} \mathcal{F}_1 \mathbf{J}_{\perp} + \eta_{\perp} \mathcal{F}_2 \mathbf{J} \times \mathbf{b} \right) , \qquad \text{(A1)}$$

where $\eta_{\perp} = m_e \nu_{ei} / (e^2 n_e)$ and $\eta_{\parallel} \approx 0.51 \eta_{\perp}$ are the same as defined previously, $\mathbf{b} = \mathbf{B}/B$ is the unit vector in the direction of the magnetic field and

$$\begin{aligned} \mathcal{F}_1(\xi) &= 1 - \frac{6.42\xi^2 + 1.84}{\Delta} , \\ \mathcal{F}_2(\xi) &= \frac{\xi \left(1.7\xi^2 + 0.78 \right)}{\Delta} , \\ \xi &= \Omega_e / \nu_{ei} , \end{aligned}$$

$$\Delta = \xi^4 + 14.79\xi^2 + 3.77 ,$$

where the above numerical coefficients are for a hydrogen plasma. In the limit $\xi \to \infty$, this expression reduces back to Eq. (15), while in the unmagnetized limit $\xi \to 0$, the functions limit to $\mathcal{F}_2 = 0$ and $\mathcal{F}_1 = 0.51$ and the standard unmagnetized result used in Sec. III B is recovered. For the Harris sheet benchmarks in Sec. III C, the last term in the generalized friction force (A1) is negligible in the y-direction, since the initial current is purely J_y and the narrow layer maintains the approximate 1D symmetry. In the limit of a neutral sheet, the current is entirely perpendicular and only the middle term contributes to force balance shown in Sec. III C. For the reconnection simulations in Sec. IV, all three terms can become important in various regions.

The generalized expression for the thermal force is

$$\mathbf{R}_T = -n_e \left(0.71 \nabla_{\parallel} T_e + \mathcal{G}_1 \nabla_{\perp} T_e + \mathcal{G}_2 \mathbf{b} \times \nabla T_e \right) , \qquad \text{(A2)}$$

where

$$\begin{aligned} \mathcal{G}_1 &= \frac{5.1\xi^2 + 2.68}{\Delta} , \\ \mathcal{G}_2 &= \frac{\xi \left(1.5\xi^2 + 3.05 \right)}{\Delta} , \end{aligned}$$

and the numerical coefficients are for hydrogen. This expression reduces back to Eq. (16) in the strongly magnetized limit $\xi \to \infty$ and also recovers the standard unmagnetized limit $\xi \to 0$. In the Harris sheet benchmarks discussed in Sec. III C, the last term in Eq. (A2) is non-negligible in the limit of weak guide field, while the first two terms do not contribute to the y-component of the force balance.

In the large and small argument limits, the reported accuracy [27] of these transport coefficient is $\sim 2\%$, however in the intermediate regime $\nu_{ei} \sim \Omega_e$ the error is considerably larger $\sim 10 - 20\%$. Furthermore, these results do not include effects due to the field inhomogeneity in the current layer, such as the electron ∇B drift.

ACKNOWLEDGMENTS

We gratefully acknowledge the support of the U.S. Department of Energy through the LANL/LDRD Program for this work. Contributions from HK were supported by the NASA Heliophysics Theory Program

[1] H. Ji, Y. Ren, M. Yamada, S. Dorfman, W. Daughton, and S. Gerhardt, Geophys. Res. Lett. **35**, L13106 (2008).
[2] P. Cassak, J. Drake, and M. Shay, Astrophys. J. **644**, L145 (2006).
[3] D. Uzdensky, Astrophys. J. **671**, 2139 (2007).
[4] D. Uzdensky, Phys. Rev. Lett. **99**, 261101 (2007).
[5] D. Biskamp, Phys. Fluids **29**, 1520 (1986).
[6] M. Ugai and T. Tsuda, J. of Plasma Phys. **17**, 337 (1977).
[7] D. Uzdensky and R. Kulsrud, Phys. Plasmas **7**, 4018 (2000).

[8] M. Yan, L. Lee, and E. Priest, J. Geophys. Res. **92**, 8277 (1992).
[9] F. Malara, P. Veltri, and V. Carbone, Phys. Fluids B **4**, 3070 (1992).
[10] N. F. Loureiro, A. A. Schekochihin, and S. C. Cowley, Phys. Plasmas **14** (2007).
[11] G. Lapenta, PRL **100**, 235001 (2008).
[12] Z. Ma and A. Bhattacharjee, Geophys. Res. Lett. **23**, 1673 (1996).
[13] P. Cassak, M. Shay, and J. Drake, Phys. Rev. Lett. **95**, 235002 (2005).
[14] A. N. Simakov and L. Chacón, Phys. Rev. Lett **101**, 105003 (2008).
[15] J. Birn, J. Drake, M. Shay, B. Rogers, R. Denton, M. Hesse, M. Kuznetsova, Z. Ma, A. Bhattacharjee, A. Otto, et al., J. Geophys. Res. **106**, 3715 (2001).
[16] M. Shay, J. Drake, B. Rogers, and R. Denton, J. Geophys. Res. **106**, 3759 (2001).
[17] M. Shay, J. Drake, and M. Swisdak, Phys. Plasmas **11**, 2199 (2004).
[18] J. Huba and L. Rudakov, Phys. Rev. Lett. **93**, 175003 (2004).
[19] A. Bhattacharjee, K. Germaschewski, and C. Ng, Phys. Plasmas **12**, 042305 (2005).
[20] M. Hesse, K. Schindler, J. Birn, and M. Kuznetsova, Phys. Plasmas **6**, 1781 (1999).
[21] P. Pritchett, J. Geophys. Res. **106**, 3783 (2001).
[22] W. Daughton, J. Scudder, and H. Karimabadi, Phys. Plasmas **13**, 072101 (2006).
[23] H. Karimabadi, W. Daughton, and J. Scudder, Geophys. Res. Lett. **34**, L13104 (2007).
[24] M. Shay, J. Drake, and M. Swisdak, Phys Rev. Lett. **99**, 15502 (2007).
[25] A. Klimas, M. Hesse, and S. Zenitani, Phys. Plasmas **15**, 082102 (2008).
[26] T. Takizuka and H. Abe, J. Comput. Phys. **25**, 205 (1977).
[27] S. Braginskii, Reviews of Plasma Physics **1**, 205 (1965).
[28] M. Rosenbluth, W. MacDonald, and D. Judd, Phys. Rev. **107**, 1 (1957).
[29] L. Landau, Phys. Z. Sowjetunion **10**, 154 (1936).
[30] F. Hinton, in *Basic Plasma Physics I*, edited by A. Galeev and R. Sudan (North-Holland, 1983).
[31] K. J. Bowers, B. J. Albright, L. Yin, B. Bergen, and T. J. T. Kwan, Phys. Plasmas **15**, 055703 (2008).
[32] G. A. Bird, Phys. Fluids **13**, 2676 (1970).
[33] D. Lemons, D. Winske, W. Daughton, and B. Albright, J. Comp. Phys., *Small-angle Coulomb Collision Model for Particle-in-Cell Simulations* **in press** (2008).
[34] N. Krall and A. Trivelpiece, *Principles of Pasma Physics* (San Francisco Press, Inc., San Francisco, CA, 1986).
[35] E. G. Harris, Nuovo Cimento **23**, 115 (1962).
[36] A. Kuritsyn, M. Yamada, S. Gerhardt, H. Ji, R. Kulsrud, and Y. Ren, Phys. Plasmas **13**, 055703 (2006).
[37] F. Trintchouk, M. Yamada, H. Ji, R. Kulsrud, and T. Carter, Phys. Plasmas **10**, 319 (2003).
[38] V. Vasyliunas, Rev. Geophys. **13**, 303 (1975).